THE ACS FORNAX CLUSTER SURVEY. IX. THE COLOR–MAGNITUDE RELATION OF GLOBULAR CLUSTER SYSTEMS[*]

Steffen Mieske[1], Andrés Jordán[2,3], Patrick Côté[4], Eric W. Peng[5], Laura Ferrarese[4], John P. Blakeslee[4],
Simona Mei[6,7], Holger Baumgardt[8], John L. Tonry[9], Leopoldo Infante[2], and Michael J. West[1]

[1] European Southern Observatory, Alonso de Cordova 3107, Vitacura, Santiago, Chile
[2] Departamento de Astronomía y Astrofísica, Pontificia Universidad Católica de Chile, Santiago 22, Chile
[3] Harvard-Smithsonian Center for Astrophysics, Cambridge, MA 02138, USA
[4] Herzberg Institute of Astrophysics, Victoria, BC V9E 2E7, Canada
[5] Department of Astronomy, Peking University, Beijing 100871, China
[6] University of Paris Denis Diderot, 75205 Paris Cedex 13, France
[7] GEPI, Observatoire de Paris, Section de Meudon, 5 Place J. Janssen, 92195 Meudon Cedex, France
[8] Argelander Institut für Astronomie, Auf dem Hügel 71, 53121 Bonn, Germany
[9] Institute for Astronomy, University of Hawaii, 2680 Woodlawn Drive, Honolulu, HI 96822, USA

ABSTRACT

We investigate the color–magnitude relation for globular clusters (GCs)—the so-called blue tilt—detected in the Advanced Camera for Surveys (ACS) Fornax Cluster Survey and using the combined sample of GCs from the ACS Fornax and Virgo Cluster Surveys. We find a tilt of $\gamma_z \equiv d(g - z)/dz = -0.0257 \pm 0.0050$ for the full GC sample of the Fornax Cluster Survey (≈ 5800 GCs). This is slightly shallower than the value $\gamma_z = -0.0459 \pm 0.0048$ found for the Virgo Cluster Survey GC sample ($\approx 11{,}100$ GCs). The slope for the merged Fornax and Virgo data sets ($\approx 16{,}900$ GCs) is $\gamma_z = -0.0293 \pm 0.0085$, corresponding to a mass–metallicity relation of $Z \propto M^{0.43 \pm 0.12}$. We find that the blue tilt sets in at masses in excess of $M \sim 2 \times 10^5 \, M_\odot$. The tilt is stronger for GCs belonging to high-mass galaxies ($M_* \gtrsim 5 \times 10^{10} \, M_\odot$) than for those in low-mass galaxies ($M_* \lesssim 5 \times 10^{10} \, M_\odot$). It is also more pronounced for GCs with smaller galactocentric distances. Our findings suggest a range of mass–metallicity relations $Z_{\rm GC} \propto M_{\rm GC}^{0.3-0.7}$ which vary as a function of host galaxy mass/luminosity, a scaling similar to that observed for dwarf spheroidal galaxies. We compare our observations to a recent model of star cluster self-enrichment with generally favorable results. We suggest that, within the context of this model, the protocluster clouds out of which the GCs formed may have had density profiles slightly steeper than isothermal and/or star formation efficiencies somewhat below 0.3. We caution, however, that the significantly different appearance of the color–magnitude diagrams (CMDs) defined by the GC systems associated with galaxies of similar mass and morphological type poses a challenge to any single mechanism, including self-enrichment, that seeks to explain generically the observed GC color–magnitude relations. We therefore suggest that the detailed (and stochastic) merger/accretion histories of individual galaxies have likely played a non-negligible role determining the distribution of GCs in the CMDs of individual GC systems.

Key words: galaxies: clusters: individual (Fornax, Virgo) – galaxies: fundamental parameters – globular clusters: general

Online-only material: color figures

1. INTRODUCTION

In recent years, deep space-based imaging, in combination with high-resolution spectroscopy of individual stars, has revealed the existence of multiple stellar populations in several globular clusters (GCs) belonging to the Milky Way (e.g., Lee et al. 1999; Bedin et al. 2004; Piotto et al. 2005, 2007; Villanova et al. 2007; Milone et al. 2008). This finding has both undermined the long-held view that star clusters are simple systems consisting of single-age, single-metallicity stellar populations and renewed interest in GC self-enrichment scenarios (e.g., Frank & Gisler 1976; Smith 1996; Gnedin et al. 2002; Parmentier & Gilmore 2001; Dopita & Smith 1986; Morgan & Lake 1989; Thoul et al. 2002; Parmentier 2004; Recchi & Danziger 2005; Caloi & D'Antona 2007; Bailin & Harris 2009).

As a complement to such studies, observations of (unresolved) GCs in galaxies beyond the Local Group offer the advantage of much larger and more homogeneous databases of GC colors and magnitudes with which to investigate overall trends between integrated GC properties and the properties of the GC systems as a whole. Observations from the *Hubble Space Telescope* (*HST*), using both Wide Field Planetary Camera 2 (WFPC2) and Advanced Camera for Surveys (ACS), have been pivotal in this area (e.g., Côté et al. 2004; Harris et al. 2006, 2009; Peng et al. 2006; Jordán et al. 2007a). One of the more surprising results to have emerged from these studies has been the discovery of a relationship between the magnitudes and colors of *individual* GCs, in the sense that GCs associated with the blue subpopulation become progressively redder at high luminosities (Harris et al. 2006, 2010; Strader et al. 2006; Mieske et al. 2006; Spitler et al. 2006; Humphrey 2009; Cockcroft et al. 2009; Forbes et al. 2010).

This relation, which is now commonly referred to as the "blue tilt," has also been detected in ground-based imaging of extragalactic GC systems (Forte et al. 2007; Wehner et al. 2008; Harris 2009) and possibly for M31 as well (Fan et al. 2009). If interpreted as a mass–metallicity relation, the tilt corresponds to a scaling with mass of $Z \propto M^{0.3-0.7}$. This is comparable to the

---

relation $Z \propto M^{0.6-0.7}$ defined by the faintest dwarf spheroidal galaxies of the Milky Way (e.g., Simon & Geha 2007; Kirby et al. 2008) which have luminous masses comparable to GCs but gravitating masses 1–2 orders of magnitude larger. Recently, Mieske et al. (2006) and Blakeslee et al. (2010) have shown that a unimodal GC metallicity distribution with an underlying mass–metallicity trend may create a color–magnitude relation with a distinct blue color peak—a consequence of the nonlinear color–metallicity relation for GCs (see also Richtler 2005; Yoon et al. 2006; Peng et al. 2006).

The most homogeneous and extensive sample of extragalactic GCs currently available is that from the ACS Virgo Cluster Survey (ACS VCS; Côté et al. 2004). From imaging of 100 Virgo cluster early-type galaxies, more than 10,000 GC candidates were identified (e.g., Peng et al. 2006; Jordán et al. 2009). In Mieske et al. (2006) and ACS VCS XIV, we examined the color–magnitude relations of these GCs. A highly significant correlation, $\gamma_z \equiv d(g-z)/dz = -0.0374 \pm 0.004$ ($Z \propto M^{0.48}$), between color and magnitude was found for the subpopulation of blue GCs in the co-added samples of the three brightest Virgo cluster galaxies (M49, M87, and M60). In general, the trend was found to be more pronounced for GCs belonging to more massive host galaxies, but there were also clear galaxy-to-galaxy differences; significant blue tilts were found for the GC systems of M87 and M60 but not for that of M49 (see also Strader et al. 2006). Peng et al. (2009) have recently confirmed the presence of a blue tilt in M87 using much deeper (50 orbit) ACS imaging in the F606 (V) and F814 (I) filters, in contradiction to a claim based on these same data that the blue tilt is an observational artifact (Waters et al. 2009).

In this paper, we analyze the color–magnitude relation of GCs in the ACS Fornax Cluster Survey (ACS FCS; Jordán et al. 2007a). This survey, which imaged 43 early-type galaxies belonging to the Fornax cluster, is nearly identical in design to the ACS VCS, although it targeted galaxies in a new and different environment. We also analyze the combined GC samples from the Fornax and Virgo surveys, to improve the overall statistics and highlight possible cluster-to-cluster differences. In what follows, we focus on four main topics: (1) the variation in the tilt slope as a function of environment, (2) the mass scale where the tilt first appears, (3) the constraints imposed on GC self-enrichment models posed by our findings, and (4) the amount of tilt that may arise from GC dynamical evolution.

2. SELECTION OF GLOBULAR CLUSTERS FROM THE ACS FORNAX CLUSTER SURVEY

The ACS FCS sample consists of 43 early-type (E, S0, dE, dE, N, dS0) members of the Fornax cluster. Each galaxy was imaged in the F475W and F850LP filters ($\approx g_{475}$ and z_{850}) for a total of 760 and 1220 s, respectively. This filter combination gives roughly a factor of 2 improvement in wavelength baseline and metallicity sensitivity compared to the "canonical" ($V - I$) color index (Côté et al. 2004). The identification of bona fide GCs from these images is performed in the size–magnitude plane as described in Peng et al. (2006) and Jordán et al. (2009). This selection procedure—which is possible because the half-light radii of GCs are marginally resolved (Jordán et al. 2005) at the distance of Fornax ($d = 20.0$ Mpc; Blakeslee et al. 2009)—greatly reduces contamination from both foreground stars and background galaxies.

The ACS images have been reduced using a dedicated pipeline that is described in Jordán et al. (2004a, 2004b, 2007a). In brief, the reductions consist of image combination, galaxy modeling, model subtraction, rejection of obvious background galaxies, and the measurement of magnitudes and sizes for candidate GCs using the program KINGPHOT (Jordán et al. 2005). The result is a catalog containing integrated g and z magnitudes, ($g - z$) colors, and half-light radii, r_h, for all candidate GCs. Magnitudes and colors are corrected for foreground extinction using the reddening maps of Schlegel et al. (1998) and extinction ratios for a G2 star as specified in Sirianni et al (2005).

To estimate the contamination by background galaxies, an identical reduction procedure was applied to 17 blank, high-latitude fields observed by ACS in the F475W and F850LP filters (see Peng et al. 2006; Jordán et al. 2009 for details). The relative distributions of contaminants and GCs in the size–magnitude plane then make it possible to assign a GC probability, $\mathcal{P}_{gc}$, to every source detected in each field. In our analysis, all sources with $\mathcal{P}_{gc} \geqslant 0.5$ are considered to be GCs. The residual contamination from background galaxies that are assigned $\mathcal{P}_{gc} \geqslant 0.5$ is negligible for this study (see Mieske et al. 2006, ACS VCS XIV in the following).

3. RESULTS

Figure 1 shows color–magnitude diagrams (CMDs) for GCs in the Fornax cluster in M_z versus ($g - z$): for NGC 1399 alone, the entire FCS sample, and the FCS sample separated by host galaxy magnitude at $M_B = -19.75$ mag. This magnitude corresponds to a stellar mass of $M_* \approx 5 \times 10^{10} M_\odot$ (Peng et al. 2008). Although somewhat arbitrary, this choice divides the GC samples into two nearly equal halves, while at the same time corresponding roughly to several noteworthy mass scales in the physics of galaxy formation, i.e., the approximate transition between "young and old" galaxies, at $M_* \sim 3 \times 10^{10} M_\odot$ (e.g., Kauffmann et al. 2003, 2004), and the division between galaxies showing central luminosity deficits and excesses in their surface brightness profiles, at $M_* \sim (5-10) \times 10^{10} M_\odot$ (Ferrarese et al. 2006a, 2006b; Côté et al. 2006, 2007). Throughout this paper, we will refer to the galaxy sample with $M_B < -19.75$ mag as the high-mass sample and that with $M_B \geqslant -19.75$ as the low-mass sample.

We use the surface brightness fluctuation distance moduli from Mei et al. (2007) and Blakeslee et al. (2009), which have an internal precision of ≈ 0.08 mag, to assign absolute magnitudes to the associated GCs. Figure 2 shows the CMDs of the full VCS sample, the combined FCS and VCS sample, and the combined FCS and VCS sample after separation into high-mass and low-mass galaxies.

3.1. KMM Fitting Procedure

Analogous to ACS VCS XIV, we apply KMM (Ashman et al. 1994) in the heteroscedastic mode to the CMDs of these subsamples, subdivided into 25 luminosity bins containing the same number of GCs. By adopting a fixed number of luminosity bins, we are able to get a straightforward comparison of the color scatter between different subsamples. The only exception is the CMD of NGC 1399 in Figure 1, for which we adopt 10 luminosity bins due to the smaller number of GCs. For each bin, KMM is used to determine the best-fit blue and red peak magnitudes of a bimodal Gaussian color distribution. In the heteroscedastic mode, we allow for
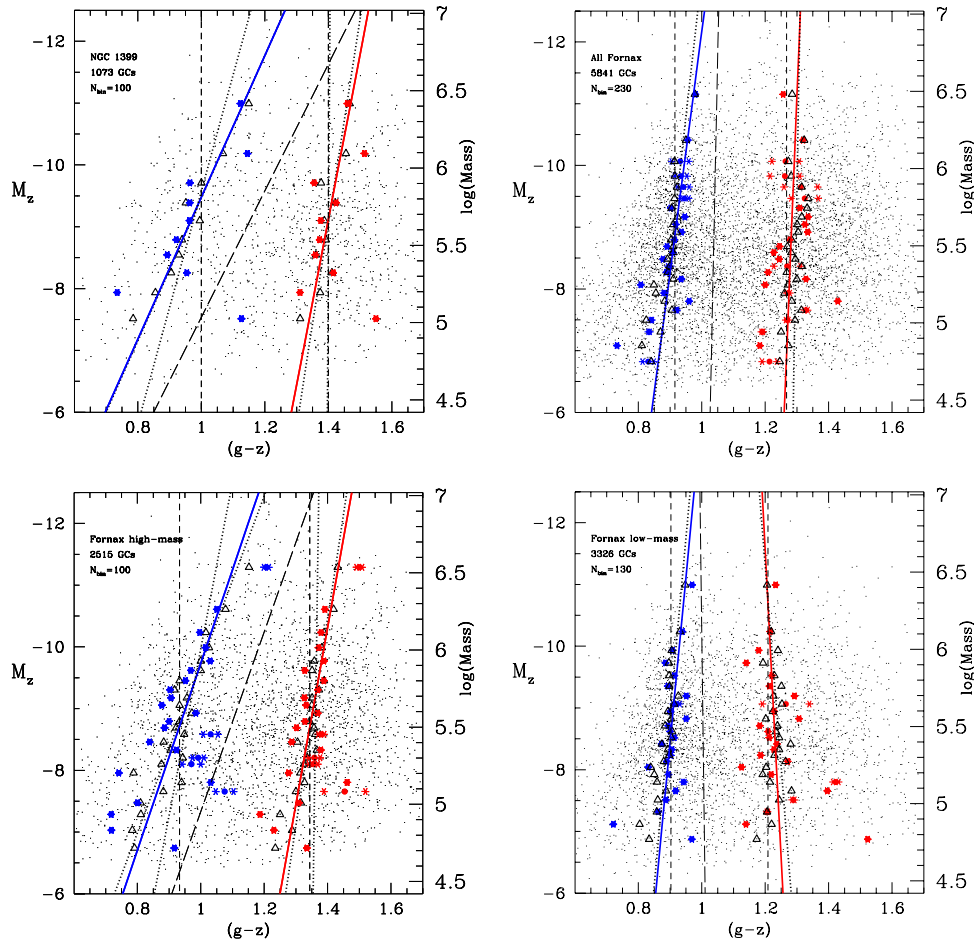
Figure 1. M_z vs. $(g - z)$ CMD for GCs detected in the ACS FCS. From top left to bottom right, the plots show (1) the GCs associated with NGC 1399, (2) all GCs in the FCS, (3) GCs belonging to `high-mass` galaxies, and (4) GCs belonging to `low-mass` galaxies. The vertical dashed lines in each panel mark the color expected for the blue and red populations based on the relation between the host galaxy magnitude and peak colors presented in Peng et al. (2006). Filled circles indicate the KMM fitting results, corresponding to the means obtained from adopting two different initial guesses (indicated by asterisks; see Section 3.1 for more details). The number of luminosity bins is 25, except for NGC 1399, where 10 luminosity bins were adopted. The solid blue and red lines indicate linear least-square fits to the KMM peak positions. The long-dashed line at intermediate colors denotes the dividing point between the blue and red peaks (i.e., the color where both blue and red peaks contribute 50% to the number counts) derived from the KMM fits. The open triangles indicate the median color of GCs blueward and redward of the dividing line. The dotted line is a fit to the median colors. For both the CMD of NGC 1399 and that of the FCS `high-mass` sample, we also show least-squares fits to the median colors blueward and redward of a magnitude-independent dividing line. This dividing line is given by the mean color of the long-dashed line between the brightest magnitude bin and $M_z = -8.1$ mag.

(A color version of this figure is available in the online journal.)

Gaussians of different widths to be fitted to the blue and red GC subpopulations.

To obtain an estimate of the uncertainty involved in the choice of the initial peak position guesses, we perform the KMM fitting in two iterations. We first run KMM using the mean peak colors of the full samples (i.e., FCS, VCS, or FCS and VCS combined) as initial guesses. From the KMM results for a given subsample, we then calculate the peak color $(g - z)_0$ averaged over all luminosity bins and calculate the dispersion, σ_0, of the peak colors around their mean. Typically, σ_0 was found to be in the range 0.05–0.1 mag. For the second iteration, we then run KMM twice, with two different initial guesses: $(g - z)_0 \pm \sigma_0$. For the final measurement, we adopt the mean of the KMM results obtained from the two initial guesses. In Figures 1 and 2, these fitted positions of the blue and red peaks are plotted over the respective CMDs. The mean is indicated by a filled circle, while the results from the two initial guesses are shown by asterisks. In most cases, the KMM results were found to be identical for the two initial guesses. We also note that for all the samples investigated in this paper, *bimodal* Gaussian color distributions

are strongly preferred over *unimodal* Gaussian distributions (confidence levels $\gtrsim$99%). Note that in ACS VCS XIV, it was shown that the KMM results are reliable for $M_z - (g - z)$, while for $M_g - (g - z)$ they are biased toward progressively bluer colors at bright luminosities (due to the depopulation of the red peak at high g-band luminosities). We therefore do not consider $M_g - (g - z)$ CMDs.

In these plots, we show as vertical dashed lines the mean color expected for the blue and red peaks based on the relation between the host galaxy magnitude and GC peak colors found by binning independent color distributions (Peng et al. 2006). The mean colors of the blue peaks agree very well with the KMM fit results in this paper. For the full VCS, and VCS plus FCS, samples, the KMM fits and median colors give a small redward offset of $\lesssim$0.05 mag for the red peak compared to the results of Peng et al. (2006), due to the slightly asymmetric shape of this peak (see Figures 2 and 5 of Peng et al. 2006).

To measure the amplitude of the tilt, we perform least-square fits of the KMM data points for the blue and red peaks as a function of magnitude, excluding GC candidates brighter
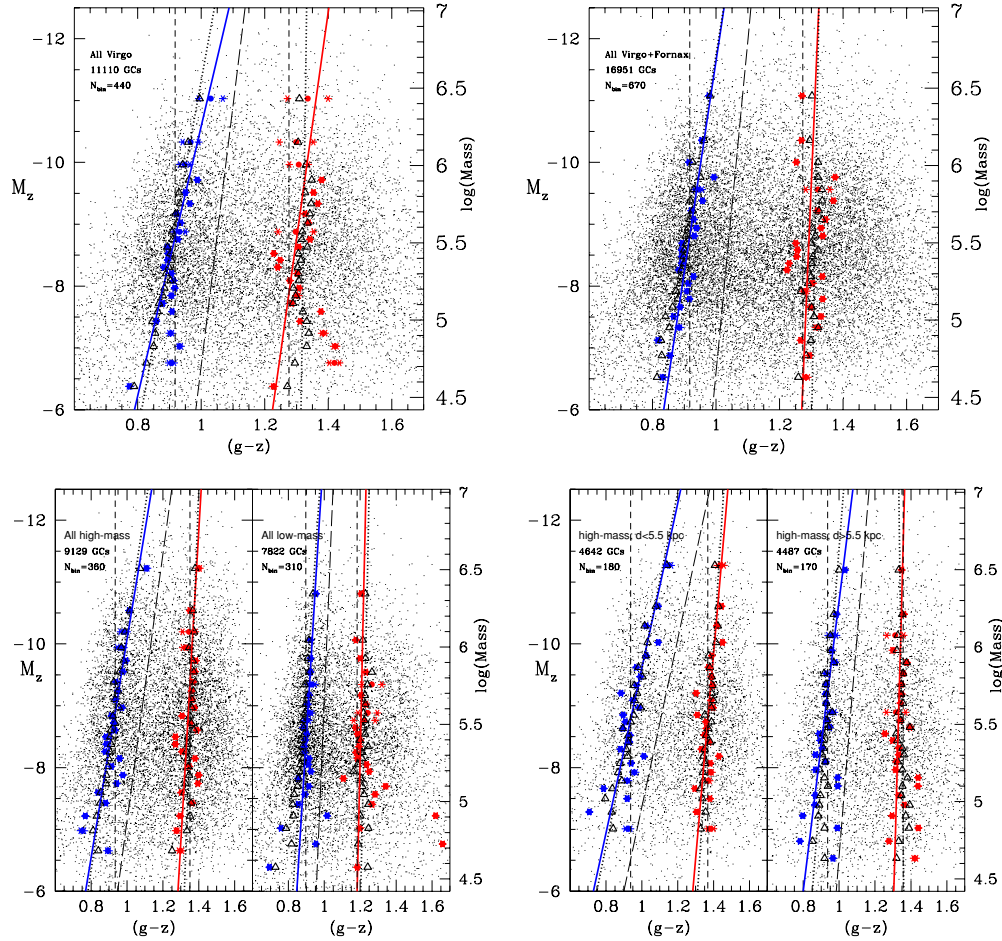
Figure 2. CMDs for various GC subsamples with results from KMM overplotted. The symbols and lines are the same as in Figure 1. Upper left panel: the full VCS sample. Upper right panel: the combined FCS and VCS sample. Lower left panel: the left portion of the diagram shows all GCs from the `high-mass` FCS and VCS galaxies, while the right portion shows GCs from the `low-mass` FCS and VCS galaxies. Note the more pronounced tilt for GCs belonging to the `high-mass` galaxies. Lower right panel: CMD showing two subsets of GCs in the `high-mass` sample, divided at a projected galactocentric distance of $d = 5.5$ kpc into inner and outer samples.

(A color version of this figure is available in the online journal.)

than $M_z = -12.5$ mag and magnitude bins fainter than $M_z = -8.1$ mag. The resulting linear relations are indicated in the CMDs of Figures 1 and 2. The errors on the fit are calculated by resampling the points using as the dispersion the observed scatter around the fitted relation. The measured slopes and errors $\gamma_z \equiv d(g - z)/dz$ are shown in Table 1. We also indicate an estimate of the corresponding mass–metallicity scaling $Z \propto M^n$. This is obtained from converting the $(g - z)$ data points to [Fe/H] using a biquadratic transformation based on Peng et al. (2006) and fitting a linear relation to the data points in magnitude–[Fe/H] space. The slope of this transformation is $\frac{\Delta[\text{Fe/H}]}{\Delta(g-z)} \simeq 5$ dex mag^{-1} in the color range of the blue peak $((g - z) \simeq 0.95$ mag$)$ and $\frac{\Delta[\text{Fe/H}]}{\Delta(g-z)} \simeq 2$ dex mag^{-1} in the color range of the red peak $((g-z) \simeq 1.35$ mag$)$. We assume a constant mass-to-light ratio over the luminosity range investigated.

As a check on the KMM fits, we calculate the slope using the median colors blueward and redward of the limiting color between the blue and red peaks. In Figures 1 and 2, the median values are indicated as open triangles and the fit to them as a dotted line. Note that we define the limiting color as the point where the contribution from the blue and red peaks is equal; this is generally different from the minimum of the color distribution. The limiting color is first determined for each

luminosity bin based on the results from KMM. We then fit a linear relation to the limiting color as a function of magnitude and use this limiting color (the long-dashed lines in Figures 1 and 2) to separate the blue and red peaks. We report the slopes of these median estimates in Table 1. These generally agree quite well with the KMM results. Only the median in the most luminous bin is somewhat bluer than the KMM result. This is because the KMM fit in the brightest bin typically shows a redward "jump" of the color distribution with respect to fainter magnitudes (see Section 3.3) due to the near-merging of the blue and red peaks, an effect that is not as apparent using the median estimate due to the smoothly changing color limit adopted for the median calculation. The blue tilt measured from the median is hence, on average, 8%–10% weaker than that measured from KMM. For the CMDs of NGC 1399 and the Fornax `high-mass` sample—which exhibit the most dramatic tilts— we also indicate the "minimum" color–magnitude relations obtained from determining the median colors blueward and redward of a magnitude-independent limiting color.

3.2. Measured Slopes for Various Subsamples

Table 1 shows that the slope obtained for NGC 1399 is quite dramatic, with $\gamma_z = -0.0878 \pm 0.0250$. This trend is

Table 1
Color–Magnitude Trends for Red and Blue GCs in ACS FCS and VCS Galaxies, Determined with KMM Fits

Sample	$\gamma_{z,\text{blue}}$	$n\ (Z \propto M^n)$	$\gamma_{z,\text{red}}$	$n\ (Z \propto M^n)$
NGC 1399 ($M_B = -20.9$)	$-0.0878 \pm 0.0250\ [-0.0863]$[a]	0.82 ± 0.23	$-0.0256 \pm 0.0050\ [-0.0215]$[a]	0.31 ± 0.12
FCS high-mass ($-22.1 < M_B < -19.75$)	$-0.0697 \pm 0.0116\ [-0.0737]$[b]	0.70 ± 0.12	$-0.0363 \pm 0.0091\ [-0.0309]$[b]	0.25 ± 0.07
FCS low-mass ($-19.75 < M_B < -16$)	$-0.0186 \pm 0.0066\ [-0.0177]$	0.28 ± 0.10	$+0.0101 \pm 0.0125\ [+0.0154]$	-0.04 ± 0.05
FCS	$-0.0257 \pm 0.0050\ [-0.0215]$	0.38 ± 0.08	$-0.0078 \pm 0.0117\ [-0.0033]$	0.03 ± 0.05
VCS	$-0.0459 \pm 0.0048\ [-0.0352]$	0.62 ± 0.08	$-0.0223 \pm 0.0095\ [-0.0026]$	0.12 ± 0.05
FCS+VCS high-mass ($-22.1 < M_B < -19.75$)	$-0.0566 \pm 0.0076\ [-0.0514]$	0.66 ± 0.09	$-0.0198 \pm 0.0099\ [-0.0123]$	0.10 ± 0.05
FCS+VCS low-mass ($-19.75 < M_B < -15.4$)	$-0.0210 \pm 0.0034\ [-0.0231]$	0.33 ± 0.06	$-0.0076 \pm 0.0087\ [-0.0072]$	0.03 ± 0.03
FCS+VCS high-mass, $d < 5.5$ kpc	$-0.0750 \pm 0.0120\ [-0.0700]$	0.76 ± 0.12	$-0.0301 \pm 0.0094\ [-0.0225]$	0.20 ± 0.07
FCS+VCS high-mass, $d > 5.5$ kpc	$-0.0428 \pm 0.0071\ [-0.0267]$	0.58 ± 0.10	$-0.0094 \pm 0.0120\ [-0.0041]$	0.04 ± 0.06
FCS+VCS	$-0.0293 \pm 0.0085\ [-0.0312]$	0.43 ± 0.12	$-0.0082 \pm 0.0190\ [-0.0034]$	0.03 ± 0.08

Notes. For the samples in Column 1 (see Figures 1 and 2 for the respective CMDs), Columns 2 and 4 give the slopes γ between $(g-z)$ and the z-band magnitudes of the blue and red GC subpopulations, determined from linear fits to the KMM peak positions. Errors are based on random resampling of the data points using their measured dispersion around the fit. Values in square brackets are the slopes determined from median colors blueward and redward of the dividing line between both populations. Columns 3 and 5 give the corresponding scaling relation in mass–metallicity space. The lower limit used in the fitting was $M_z = -8.1$ mag for all samples.
[a] Slopes from median colors at magnitude-independent color division: $\gamma_{z,\text{blue}} = -0.0551$, $\gamma_{z,\text{red}} = -0.0009$ (see Figure 1).
[b] Slopes from median colors at magnitude-independent color division: $\gamma_{z,\text{blue}} = -0.0331$, $\gamma_{z,\text{red}} = -0.0003$ (see Figure 1).

significant at roughly the 3.5σ level. In mass–metallicity space, this corresponds to a scaling relation of $Z \propto M^{0.82\pm0.23}$. The morphology of the CMD of NGC 1399 shows that this strong slope originates from a near-merging of the blue and red peaks at the highest luminosities (see also Dirsch et al. 2003; Bassino et al. 2006). Nevertheless, we emphasize that KMM still gives a confidence level of 98%–99% for preferring a bimodal Gaussian over a unimodal Gaussian for the brightest bins.

When considering the full sample of GCs from the FCS, we find a shallower but still highly significant tilt of $\gamma_z = -0.0257 \pm 0.0050$. This is weaker than the tilt $\gamma_z = -0.0459 \pm 0.0048$ found for the full VCS data set (see Figure 2 and Table 1). For the subsample of GCs belonging to the high-mass FCS galaxies, we find a slope of $\gamma_z = -0.0697 \pm 0.0116$. GCs belonging to the low-mass FCS galaxies show a rather weaker slope of $\gamma_z = -0.0186 \pm 0.0066$. This result for the FCS confirms the finding from ACS VCS XIV that the slope becomes weaker for GCs belonging to less luminous galaxies. This also holds when considering the alternative fit results based on median colors and even when using the "minimum" slope derived in the previous subsection. To reinforce this point, the bottom left panel of Figure 2 shows the combined FCS and VCS sample, subdivided into high-mass and low-mass galaxies. The tilt for the high-mass sample is $\gamma_z = -0.0566 \pm 0.0076$, almost 3 times steeper than that for the low-mass sample, $\gamma_z = -0.0210 \pm 0.0034$. The two slopes are inconsistent with each other at the 4.3σ level and imply a range of mass–metallicity scalings $Z \propto M^{0.3-0.7}$ as a function of galaxy luminosity/mass. For the full sample of GCs from the two surveys (Figure 2), we find a slope of $\gamma_z = -0.0293 \pm 0.0085$. This slope, which is, as expected, intermediate to those found for the FCS and VCS samples, corresponds to $Z \propto M^{0.43\pm0.12}$.

The bottom right panel in Figure 2 shows two GC subsets in the high-mass galaxies from the combined FCS and VCS sample, separated at a projected galactocentric distance $d = 5.5$ kpc (corresponding to ≈ 0.25–1 R_e for these galaxies; Ferrarese et al. 2006a, 2010). The slope found for the *inner sample* is $\gamma_z = -0.0750 \pm 0.0120$, significantly higher than the value $\gamma_z = -0.0428 \pm 0.0071$ found for the *outer sample*. The tilt difference is even more pronounced when using the alternative median fitting. This confirms the findings from ACS

VCS XIV that the tilt is most significant for GCs lying at small projected galactocentric distances.

3.2.1. M49 Revisited: Blue Tilt Differences Between High-luminosity Galaxies

Both in ACS VCS XIV and in Strader et al. (2006), it was noted that no blue tilt was detected for the brightest Virgo cluster galaxy M49. To put this intriguing result into perspective, we compare in Figure 3 the CMDs for NGC 1399 (Fornax), M49 (Virgo), and M87 (Virgo). We choose a subdivision into 15 bins for the KMM fitting to all three galaxies. Both NGC 1399 and M87 show significant blue tilts (ACS VCS XIV; Strader et al. 2006; Peng et al. 2009), while M49 apparently shows no obvious color–magnitude relation. Comparing the overall morphology of the CMDs, it is clear that in the case of M49, the lack of bright, intermediate-color GCs is at least partly responsible for the lack of a tilt; that is, the blue peak in M49 is narrow and there is a clear gap between the blue and red peaks over the entire magnitude range.

This difference relative to M87 and NGC 1399 is difficult to reconcile within a scenario where a GC mass–metallicity relation is created entirely by a single mechanism operating within individual GCs (e.g., self-enrichment; see below). In all likelihood, the detailed accretion and merger histories of individual galaxies will also play a role in establishing the distribution of GCs within the color–magnitude plane.

3.3. A Luminosity/Mass Threshold for the Blue Tilt

It has been suggested that the blue tilt is driven mainly by GCs that are brighter than the GC luminosity function turnover magnitude (e.g., Harris et al. 2006; ACS VCS XIV; Peng et al. 2009). To investigate the luminosity/mass threshold of the blue tilt, we show in the upper left panel of Figure 4 the dependence of slope γ_z on the lower magnitude limit used in the fitting procedure. In doing so, we have fitted a linear relation to the KMM peak results for the combined Fornax and Virgo samples, subdivided into high-mass and low-mass host galaxies (the bottom left panel of Figure 2). The faint magnitude cutoff has been varied from $M_{z,\text{cut,faint}} = -7.5$ to -9.5 mag.

For the high-mass sample, there is a notable trend for the derived slope to *increase steadily from* $\gamma_z \simeq -0.045$ *to* -0.075

NGC 1399
1073 GCs
$N_{bin}=70$

M 49
764 GCs
$N_{bin}=50$

M 87
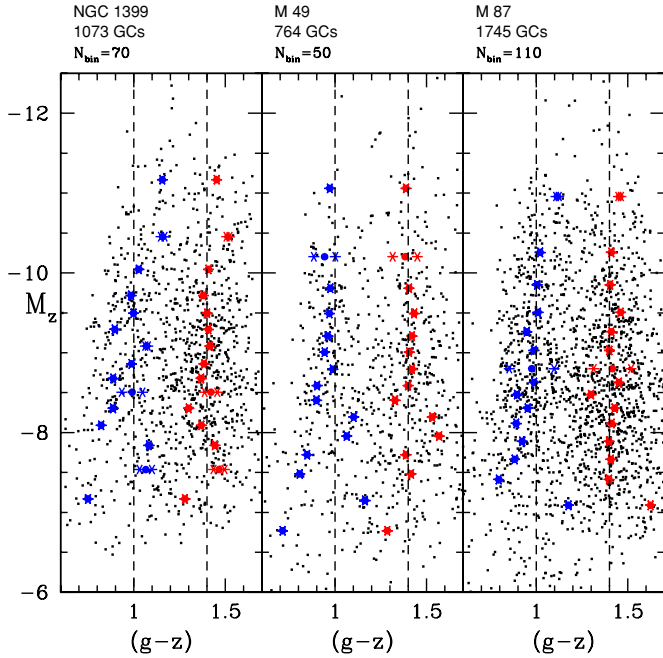1745 GCs
$N_{bin}=110$

Figure 3. Distribution of GCs in the CMD for three giant elliptical galaxies NGC 1399 (Fornax), M49 (Virgo), and M87 (Virgo). Results from KMM are overplotted for a fixed number of 15 luminosity bins. Note the absence of a blue tilt in M49, possibly due to the lack of intermediate-color GCs at luminosities of $M_z \lesssim -10.5$ mag.

(A color version of this figure is available in the online journal.)

as the faint cutoff magnitude is varied from $M_{z,\mathrm{cut,faint}} = -7.5$ *to* -9.5 *mag*. This may be a signature of a nonlinear color–magnitude relation at the upper end of the GC luminosity function. The open circles in this plot show the change in slope when the brightest magnitude bin, at $M_z = -11.2$ mag, is excluded. In this case, the slope is roughly constant at $\gamma_z \simeq -0.045$, a value of that is largely independent of the faint cutoff for $M_{z,\mathrm{cut,faint}} \lesssim -8.0$. Hence, the steepening slope seems to be due to the increasing weight of the very brightest GCs, with $M_z \lesssim -11$ mag.

We conclude from this exercise that the blue tilt is firmly in place above $M_{z,\mathrm{cut}} \approx -8$ mag $((1.5–2) \times 10^5 M_\odot)$ and further steepens at $M_z \lesssim -11$ mag $(\gtrsim (2–3) \times 10^6 M_\odot)$. Nevertheless, the upper left panel of Figure 4 shows clearly that the strong blue tilt for GCs in the high-mass sample is not driven by the brightest GCs alone since the open circles are consistently above the crosses.

This plot also demonstrates once again that the blue tilt is more pronounced in the Virgo data. In this context it is crucial to note that the GCs in the VCS sample originate, on average, from more luminous galaxies than in the FCS sample (see the upper right panel of Figure 4): there is a difference of 0.5–1.0 mag in the host galaxy magnitude. The GC number ratio of the high-mass to low-mass samples is 43:57 for Fornax, but 60:40 for Virgo. Given the overall stronger tilt found for the high-mass samples, this difference in host galaxy distribution appears to be the root cause of the stronger tilt found using the Virgo sample.

In the bottom panels of Figure 4, we investigate in detail how γ_z changes as a function of the *bright* cutoff magnitude. We consider the high-mass and low-mass subsamples in the combined FCS and VCS sample and keep $M_z = -8.1$ mag fixed as the faint cutoff. In order to obtain a finer grid of

peak positions at bright luminosities, we (1) apply a varying bright cutoff to the individual GC data points, instead of a cut to the KMM peak positions as above for the faint magnitude cutoff,[10] and (2) adopt a slightly smaller bin size of 200 GCs. We then vary the upper cutoff in steps of 0.25 mag between $M_z = -12.5$ mag and $M_z = -8.5$ mag. For each restricted sample, we fit red and blue KMM peaks. In the bottom left panel, we overplot the KMM peak results for all adopted bright GC magnitude limits. For the high-mass sample, the peak positions of the blue GC population "bend" slightly at higher GC masses. In the bottom right panel of Figure 4, this behavior is quantified by plotting γ_z as a function of the upper cutoff magnitude. For GCs belonging to the high-mass sample, the slope is within the errors independent of the upper cutoff for -11 mag $< M_{z,\mathrm{cut,bright}} < -9$ mag, but increases somewhat from $\gamma_z = -0.040$ to $\gamma_z = -0.052$ when including also the brightest GCs with -12.5 mag $< M_z < -11$ mag. For GCs in the low-mass sample, no steepening for bright GCs is apparent.

In summary, the tilt becomes stronger for the most massive GCs ($\gtrsim (2–3) \times 10^6 M_\odot$) belonging to the high-mass sample, but not for the GCs in the low-mass sample.

3.4. Evidence for a Red Tilt?

We now examine the evidence for a "red tilt" in the data, i.e., a color–magnitude relation for the subpopulation of red GCs. Table 1 shows that there is indeed a 2σ–3σ effect that is detectable in the high-mass samples, indicating a gentle mass–metallicity relation of $Z \propto M^{0.1–0.2}$. There is, however, no significant red tilt detected in the full sample of all GCs. Given this and the fact that the color distribution in the red peak is generally asymmetric (see Figures 2 and 5 of Peng et al. 2006), the evidence for a red tilt should still be considered preliminary. We note that a weak tilt is broadly consistent with the GC self-enrichment scenario, where the pre-enrichment level of red (metal-rich) GCs is significantly higher than that of the blue (metal-poor) GCs, thereby making the detection of any self-enrichment more difficult (e.g., ACS VCS XIV; Strader & Smith 2008; Bailin & Harris 2009).

We conclude this section with a note of caution regarding the detection of tilts, red or blue: the colors of individual GCs typically scatter significantly about the individual peak positions by 0.1–0.2 mag. This scatter—likely caused by stochastic variation in the GC pre-enrichment level—will allow the detection of any mass–metallicity trend only for systems of at least a few hundred GCs. The significance of the blue tilt detection in the GC system of the disk galaxy NGC 5170 (Forbes et al. 2010)—which has about 600 GCs—is $\sim 3\sigma$, showing that it would be difficult to detect subtle tilts in poorer GC systems like that of the Milky Way (see also Strader & Smith 2008; Bailin & Harris 2009).

4. DISCUSSION

In ACS VCS XIV, it was shown that neither stochastic fluctuations within the stellar CMDs, contamination of the GC samples by tidally stripped nuclei, nor the accretion of GCs like those found in present-day galaxies could fully explain the observed color–magnitude relations. Subsequently, in Mieske & Baumgardt (2007), it was shown through N-body simulations that field star capture is much too inefficient to account for any

---

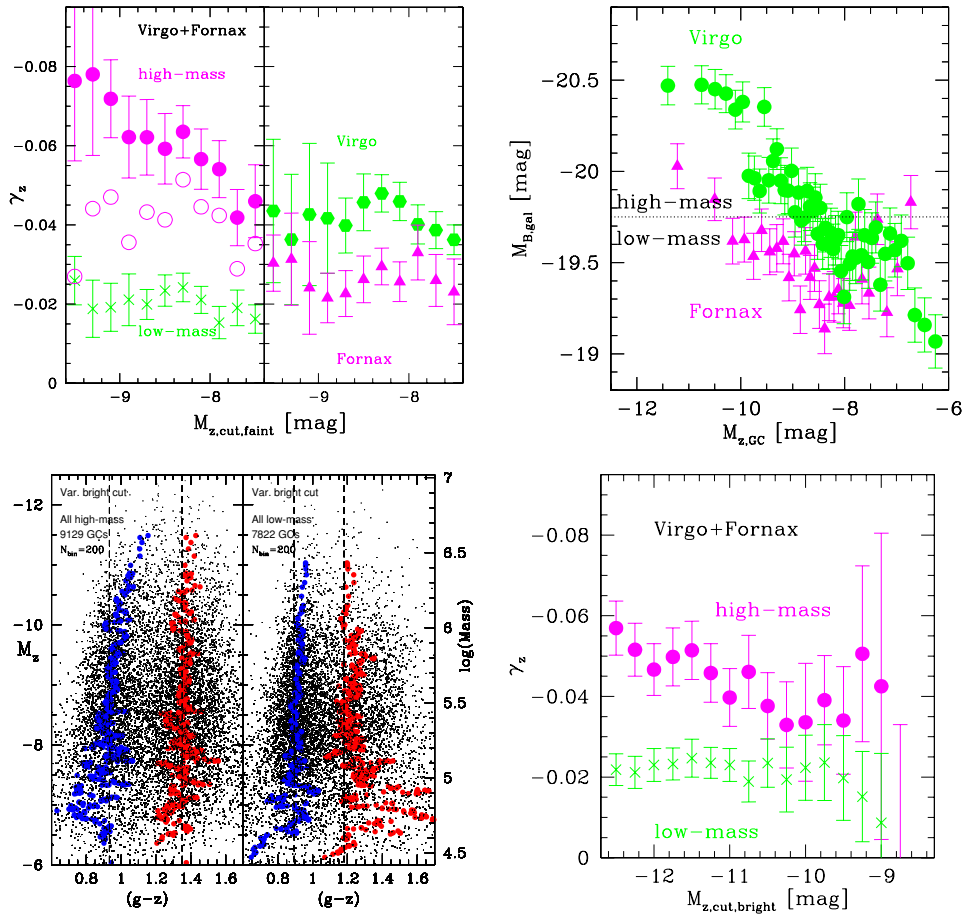[10] The latter is adequate due to the much denser spacing of magnitude bins at fainter magnitudes.

Figure 4. Dependence of blue tilt on the GC mass range used in the analysis. Upper left panel: variation in the blue tilt slope, γ_z, as a function of the faint magnitude cutoff, $M_{z,\mathrm{cut,faint}}$. In the left portion of the diagram, the filled magenta circles (green crosses) indicate the combined FCS and VCS sample restricted to GCs belonging to high-mass (low mass) galaxies. Open circles indicate a fit to the high-mass sample when disregarding the brightest GC magnitude bin at $M_z = -11.2$ mag (see the bottom left panel of Figure 2). In the right portion of the diagram, the filled green circles show the full VCS sample, while the filled magenta triangles show the full FCS sample. Upper right panel: the mean host galaxy magnitude for GCs is plotted vs. GC magnitude, for a bin size of 200 GCs. Filled green circles indicate the full VCS sample, while filled magenta triangles indicate the full FCS sample. The limiting magnitude between high-mass and low-mass galaxies is indicated by a horizontal dotted line. Bottom left panel: the CMDs of GCs belonging to high-mass and low-mass galaxies. This is identical to the bottom left panel of Figure 2, but with an overplotted complementary set of KMM fit results, in which we have varied the bright magnitude limit of the GC samples between $M_z = -12.5$ mag and $M_z = -8.5$ mag in steps of 0.25 mag. For each restricted sample, we run KMM and plot the fitted peak results. Bottom right panel: this plot is based on the fits in the bottom left panel. It shows the slope γ_z fitted to the KMM peak positions as a function of the *bright* magnitude cutoff, $M_{z,\mathrm{cut,bright}}$, applied to the GC samples. The faint limiting magnitude used in the fitting is $M_z = -8.1$ mag.

(A color version of this figure is available in the online journal.)

tilt. In this section, we examine the self-enrichment scenario put forward by Bailin & Harris (2009), including new constraints imposed on this scenario by the observed trends with environment (Section 4.1). We then quantify the effects of GC dynamical evolution on the distribution of clusters within the color–magnitude plane (Section 4.2).

4.1. Constraints on Self-enrichment Scenarios

Models for the self-enrichment of star clusters have a long history (see, e.g., Frank & Gisler 1976; Smith 1996; Gnedin et al. 2002; Parmentier & Gilmore 2001; Dopita & Smith 1986; Morgan & Lake 1989; Thoul et al. 2002; Recchi & Danziger 2005; Parmentier 2004; Baumgardt et al. 2008) and they appear to offer a promising explanation for the blue tilt. The mass–metallicity relations as reported in this paper range from $Z \propto M^{0.3}$ to $\propto M^{0.7}$. This overlaps with the $Z \propto M^{0.6-0.7}$ relations found for dwarf spheroidal galaxies (e.g., Simon & Geha 2007; Kirby et al. 2008) which have luminosities, metallicities, and central velocity dispersions that are similar

to those of GCs (although the latter appear to be baryon, rather than dark matter, dominated).

In Strader & Smith (2008), Bailin & Harris (2009), and Harris et al. (2010), the self-enrichment scenario of star clusters is discussed with a focus on the blue tilt. The underlying assumption is that self-enrichment by SNII ejecta starts to become efficient when the energy output by SNII is comparable to the binding energy of the cluster's primordial gas cloud. This implicitly assumes that 100% of the SN ejecta energy is converted to kinetic energy of the cloud gas (see Tenorio-Tagle et al. 2007 for an alternative view). Bailin & Harris (2009) parameterize the ability for self-enrichment of a protocluster cloud based on the metal-retention fraction, f_Z (Equation (7) of their paper):

$$\log Z_c/Z_\odot = \log(10^{Z_\mathrm{pre}} + 10^{0.38+\log f_* f_Z}), \quad (1)$$

where f_* denotes the star formation efficiency. The particular value of 0.38 used in the exponent of the second term is determined by the SN yield. For the metal-retention fraction,
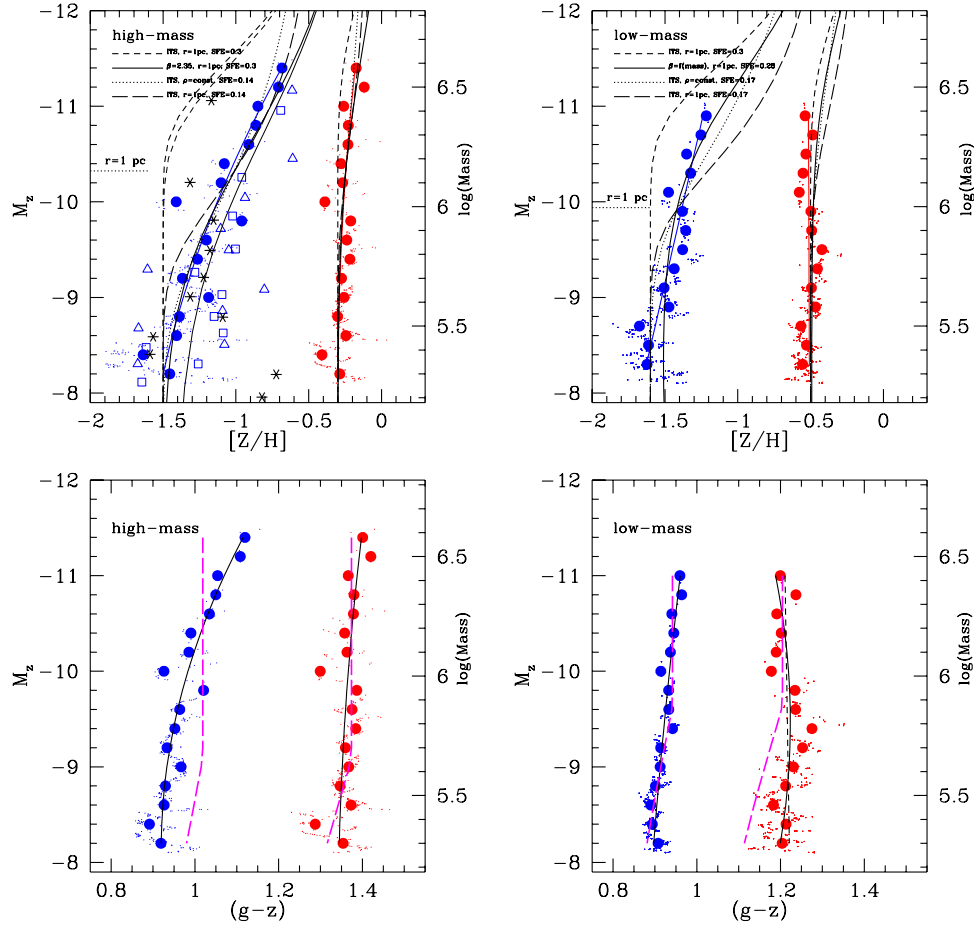
Figure 5. Comparison of the observed tilt (blue and red) to predicted changes of metallicity/color caused by self-enrichment (top panels) and dynamical evolution (bottom panels). We consider separately the GC subsamples belonging to `high-mass` and `low-mass` host galaxies. The filled blue and red solid circles correspond to the mean GC metallicity/color in magnitude bins of 0.2 mag also shown in the bottom left panel of Figure 4. The colors $(g - z)$ have been converted to metallicity $[z/H]$ using the biquadratic transformation of Peng et al. (2006). In the top left panel, the open triangles indicate the individual peak positions for NGC 1399, the squares indicate M87, and the asterisks show M49. Top panels (*a test of self-enrichment*): the solid blue and red curves indicate quadratic fits to the KMM data points while the black curves are predictions from the self-enrichment model of Bailin & Harris (2009) for various sets of model parameters, as indicated in the plot legend. The reference model adopted by Bailin & Harris (2009) is indicated by the short-dashed curve. This particular model predicts self-enrichment to appear at an order of magnitude larger mass than is observed. The thin short-dashed and thin solid lines are a variation of the respective thick line models, assuming a constant mass loss of $\Delta = 3 \times 10^5 \, M_\odot$ to have occurred for all clusters. Bottom panels (a test of dynamical evolution): the solid curves are quadratic fits to the observed color–magnitude data points. The long-dashed magenta curves indicate the expected color change due to dynamical evolution according to the predictions from Kruijssen & Lamers (2008). For the red peak at `low-mass` galaxies, the short-dashed line also shows a linear fit to the plotted data points.

(A color version of this figure is available in the online journal.)

Bailin & Harris derive (Equation (28) of their paper)

$$f_Z = \exp\left(-\frac{E_{\rm SN} f_* r_t}{10^2 \, M_\odot G M_c}\right). \qquad (2)$$

This expression holds for the assumption of a 3D mass density profile of the protocluster cloud that falls off as $\rho \propto r^{-2}$ (i.e., an isothermal sphere), with r_t being the truncation radius. In this equation, $E_{\rm SN}$ is the typical energy released by a single SNII ($= 10^{51}$ erg) and M_c is the mass of the protocluster cloud. A Salpeter-like stellar mass function at the high-mass end is assumed. (Note that the present-day cluster mass is linked to the protocluster cloud mass via the relation $M_{c,{\rm today}} = M_c f_*$.) For a more general density profile $\rho \propto r^{-\beta}$ with $\beta \neq 2$, it holds for f_Z (Equation (36) of their paper):

$$f_Z = \left[1 - \frac{E_{\rm SN} f_* r_t (2 - \beta)}{10^2 \, M_\odot G M_c}\right]^{\frac{3-\beta}{2-\beta}}. \qquad (3)$$

Equations (2) and (3) show that the primordial star formation efficiency, f_*; the protocluster mass–radius relation; and density

profile, ρ, will determine the self-enrichment capability of a given cluster. Our aim is to constrain these parameters based on the observed GC mass–metallicity relation. To this end, we plot in the top panels of Figure 5 GC metallicity versus absolute magnitude and mass, separated into `high-mass` and `low-mass` samples. The $[z/H]$ values are obtained directly from converting the $(g - z)$ data points to [Fe/H] using the biquadratic transformation based on Peng et al. (2006). We also show separately the data for the three high-luminosity galaxies NGC 1399, M49, and M87 (see Section 3.2.1).

Figure 5 shows the expected behavior of $\log Z_c/Z_\odot$ as a function of mass for various choices of model parameters. The short-dashed curve corresponds to the reference model adopted by Bailin & Harris (2009; see also Harris et al. 2010). For this model, the density profile is taken to be an isothermal sphere with a mass-independent truncation radius of $r_t = 1$ pc and a star formation efficiency of $f_* = 0.3$ (e.g., Boily & Kroupa 2003; Lada & Lada 2003; Baumgardt et al. 2008).

This particular set of model parameters does not reproduce the data for either the `high-mass` or the `low-mass` sample.

Most notably, the observations point to an onset of the blue tilt at $\approx 2 \times 10^5\ M_\odot$, while the reference model predicts self-enrichment to become important only above $\approx 2 \times 10^6\ M_\odot$. Moreover, the relation between mass and metallicity predicted by the model in the self-enrichment mass regime is $Z \propto M^{1.0}$–$M^{1.1}$. This is significantly steeper than the observed relation of $Z \propto M^{0.3}$–$M^{0.7}$.

Thus, the data require a lower mass for the onset of self-enrichment than in the reference model, but at the same time, a weaker scaling between metallicity and mass in the self-enrichment regime. One way of achieving this is to assume a radial density profile that is steeper than an isothermal sphere: Figure 5 shows that the particular choice of $\beta = 2.35$ matches very well the observed mass–metallicity scaling for the `high-mass` sample. For such a profile, self-enrichment is able to start at lower cloud masses due to the deeper potential well in the cloud center, but its efficiency increases more gradually with increasing cluster mass (given that only a small fraction of gas is located close to the edge of the protocluster cloud). For the `low-mass` sample, the data require a variation of β with cloud mass in the sense that lower mass clouds have a steeper profile than higher mass clusters; the shallower tilt for this sample can otherwise not be reproduced. The solid curve in Figure 5 corresponds to the particular choice of $\beta = 2.3 + 0.23[6.2 - \log(\mathrm{mass})]$.

An alternative way to match the observations for the `high-mass` sample is to adopt a lower star formation efficiency of $f_* \simeq 0.15$. This implies that the progenitor cloud for a GC of a given mass was twice as massive as in the reference model, yielding a correspondingly larger metal-retention fraction, and hence, a lower *present-day* onset mass for self-enrichment. At the same time, the choice of a lower f_* reduces the overall efficiency of self-enrichment, i.e., the slope between $[z/H]$ and mass (Equation (1)). For the `low-mass` sample, however, the curves with lower star formation efficiency do not reproduce the observed scaling of metallicity with mass.

It is important to bear in mind that the assumption of a constant cloud radius is not necessary to reproduce the observations. Figure 5 shows that clouds with constant density (i.e., $r \propto M^{1/3}$) can also have levels of self-enrichment that are in agreement with the observations.

Finally, we note that radiative feedback from massive stars also contributes to regulating star formation, with the total radiative energy input from OB stars into the interstellar medium being more than an order of magnitude lower than the energy injected by SNII (Baumgardt et al. 2008). Despite the lower amount of energy involved, radiative feedback may be an important factor for halting star formation in massive clusters (e.g., Krumholz & Matzner 2009; Fall et al. 2010) in the few million years before the first SNII explode. This effect is not considered in the self-enrichment scenario discussed in this paper, since we focus on the reprocessing of metals ejected by SNII, which dominate the budget of metal-enriched material in a star cluster.

4.1.1. Environmental Dependence

We have shown that the mass–metallicity scaling relation, and the difference between GCs in `high-mass` and `low-mass` samples, may be explained if the density profiles of the protocluster clouds are generally steeper than isothermal spheres and if the density profiles for the protocluster clouds in the `low-mass` sample depended weakly on mass. Another effect that may contribute to the observed trends is that, for larger cluster masses, an

increasing fraction of protocluster clouds with low star formation efficiency survive their formation (Baumgardt et al. 2008). This is possible since, for higher mass clusters, gas expulsion will tend to happen more adiabatically and the tidal radius is larger, so that clusters will have more room for expansion following gas expulsion. This possibility is also supported by the finding of Baumgardt et al. (2008) that in order to turn a power-law cluster mass function into the commonly observed log-normal one (e.g., Jordán et al. 2007b and references therein), a larger fraction of high-mass clusters has to survive gas expulsion. Environmental variations in the importance of these effects are certainly conceivable, e.g. in the sense that metal retainment is favored in the central parts of high-mass galaxies with external pressure confinement, different from regions in lower mass galaxies with a weaker external pressure (e.g., Parmentier 2004; Recchi & Danziger 2005). These variations may well influence the resulting mass–metallicity relation of GCs.

However, such smooth trends can hardly explain the gross differences between the GC CMD morphology for galaxies of similar morphological type and luminosity, as is the case for M49, M87, and NGC 1399 (Figures 3 and 5). Instead, these differences may indicate that individual merger or accretion events have altered their GC populations (e.g., Côté et al. 1998 or Hilker et al. 1999) and hence contributed to modulating the blue tilt. This modulation might take the form of intermediate-age GCs formed in gas-rich mergers, the dissipationless accretion of GCs belonging to gas-poor galaxies, or both (see the reviews of West et al. 2004; Brodie & Strader 2006).

An alternative explanation for the variations in the color–magnitude relations among different subsamples is considered by Blakeslee et al. (2010). These authors show that the nonlinear relationship between the GC color and metallicity may lead to different tilts in color space between samples of different mean metallicity, even though the underlying GC mass–metallicity relations may be quite similar. In this paper, we adopt a color–metallicity transformation based on 95 GCs in the Milky Way, M49, and M87 (Peng et al. 2006), the same data set which is also adopted for the color–metallicity transformation by Blakeslee et al. (2010). Since we do see a difference in the mass–metallicity relation between GCs in `high-mass` and `low-mass` galaxies, not only in color–magnitude space, it appears likely that the effect considered by Blakeslee et al. is in our case not the only cause for the environmental variation. An important step forward in this context would be to obtain accurate spectroscopic metallicity measurements for an expanded sample (e.g., Cohen et al. 1998, 2003) of GCs in the Virgo and Fornax galaxies that define the tilt and its variations.

4.2. Color Effects from Dynamical Evolution

Having constrained the conditions under which self-enrichment can reproduce the observed blue tilt, it is worth exploring the extent to which color changes due to dynamical evolution of GCs may also contribute to shaping the observed trends. In the context of the environmental variations of the tilt, this issue is worth considering in some more detail since the dynamical evolution of star clusters is known to depend strongly on the external tidal field and hence varies as a function of environment.

Three recent studies investigate the effects of tidal dissolution of star clusters on their integrated colors (Kruijssen & Lamers 2008; Anders et al. 2009; Kruijssen 2009), based on the N-body star cluster simulations of Baumgardt & Makino (2003). Of these three studies, Anders et al. (2009) and Kruijssen

(2009) perform a more sophisticated treatment of the evolution of the stellar mass function change with time, resulting in smaller predicted color changes than that presented in the more simplified treatment in Kruijssen & Lamers (2008). Both studies predict star cluster colors at a determined age and metallicity as a function of the ratio t_{dyn} of the current age to dissolution time. Generally, color changes start to set in after ~ 0.4 dissolution timescales.

To determine whether these changes can be responsible for the tilt, we estimate the amount of color change that has occurred in the GCs of the combined VCS and FCS sample. We adopt a z-band mass-to-light ratio of $M/L_z = 1.5$, independent of the $(g - z)$ color (Jordán et al. 2007b). As the fractional dynamical age, t_{dyn}, we define the ratio of the current age to the dissolution time. In the context of the GC dissolution scenario discussed in Jordán et al. (2007b), this can also be expressed as the ratio of the present-day mass to primordial mass. Using the present-day mass, $M_{present}$, and the accumulated mass loss, Δ, we find

$$t_{dyn} = 1 - \frac{M_{present}}{M_{present} + \Delta}. \qquad (4)$$

We assume Δ to be equal for all GCs in a given host galaxy, adopting $\Delta = 3 \times 10^5 \, M_\odot$ for `high-mass` galaxies and $\Delta = 5 \times 10^5 \, M_\odot$ for `low-mass` galaxies (see, e.g., Figure 16 of Jordán et al. 2007b). In the bottom panels of Figure 5, we show the `KMM` peak positions fitted to the CMDs of GCs from the combined FCS and VCS `high-mass` and `low-mass` samples. We also show quadratic fits to the `KMM` peak positions. In each luminosity bin we calculate the mean GC mass, the mean host galaxy magnitude and adopt Δ in Equation (4) accordingly, yielding an average t_{dyn} for the GCs in each luminosity bin. We then calculate an estimate for the color change at each luminosity bin, adopting the predictions by Kruijssen & Lamers (2008) in the V and I bands as a function of t_{dyn}, which serve as an upper limit to the true expected color change due to their simplified treatment of mass function exchange (see above). We use $\delta(V - I)/\delta(g - z) = 0.521$ (Peng et al. 2006) to convert to $(g - z)$ colors. The results are indicated by the long-dashed magenta lines. It is apparent that non-negligible color changes are expected for only the low-luminosity GCs: for $M_z \gtrsim -9.0$ mag in the `high-mass` sample and $M_z \gtrsim -9.5$ mag for the `low-mass` sample. Moreover, the predicted strong changes in the red peak for the `low mass` do not at all agree with the observational data. This comparison thus supports the relatively small color changes predicted by Anders et al. (2009) and Kruijssen (2009); we therefore conclude that dynamical evolution may be responsible for a weak color–magnitude trend among low-mass GCs, but certainly not for the strong tilt exhibited by the more massive clusters.

We also note that the mass loss of star clusters only has a very small effect on the self-enrichment estimates presented in the previous section. This is illustrated by two example self-enrichment model calculations in the upper left panel of Figure 5. The thin short-dashed and thin solid line show the respective thick line model variations assuming a constant mass loss of $\Delta = 3 \times 10^5 \, M_\odot$ to have occurred for all clusters. The effect on the reference model by Bailin & Harris is negligible, and the effect for the model variations that fit the data corresponds to a 10%–15% change in slope. A 0.15 dex lower pre-enrichment metallicity is required for the predictions that include mass loss to match the predictions without mass loss.

5. CONCLUSIONS

A color–magnitude relation for metal-poor GCs—the "blue tilt"—is now a well-established observational result. From a CMD analysis based on a sample of $\approx 17,000$ GCs detected in the ACS VCS and ACS FCS, we identify a clear environmental variation in the slope of the GC color–magnitude relation, i.e., the slope of the color–magnitude relation is largest for the highest-mass galaxies. Nevertheless, we confirm that there are real, galaxy-to-galaxy differences in the amount of tilt at comparable galaxy luminosity and mass; for example, M87 and NGC 1399 show significant blue tilts, while M49 does not (Mieske et al. 2006; Strader et al. 2006).

A comparison to predictions from models of GC self-enrichment (Bailin & Harris 2009) suggests that this mechanism offers a promising explanation for the observed relation and may be able to constrain the conditions under which star formation took place in protocluster clouds. Within the context of this model, the observed shape of the color–magnitude relation suggests that protocluster clouds had density profiles somewhat steeper than isothermal in the highest-mass galaxies ($\beta \approx 2.3$). For the lower mass galaxies, a weak mass dependence for the structure of the protocluster clouds is required to match the observations (with β in the range $2.5 \gtrsim \beta \gtrsim 2.2$ for masses $10^{5.5} \lesssim M/M_\odot \lesssim 10^{6.5}$). This interpretation, however, is not unique. Other variants on this same basic picture also appear consistent with the observations, including models in which the clouds have constant density ($r \sim M^{1/3}$) and/or relatively low star formation efficiencies of 0.15–0.20.

However, we point out that the significant differences in the detailed CMDs for some galaxies of similar mass and morphological type pose a challenge to single generic mechanisms, such as self-enrichment, that attempt to explain GC color–magnitude relations. These differences suggest that the detailed (and stochastic) merger/accretion histories of individual galaxies will play a role shaping the appearance of overall GC CMDs.

We conclude that further insights into the blue tilt phenomenon now await optical spectroscopy for large, representative GC samples covering the upper 3–4 mag of the GC luminosity function, where the color–magnitude relation is most apparent. At the distances of the Fornax and Virgo clusters, this corresponds to apparent magnitudes of 21 mag $\lesssim V \lesssim 24.5$ mag, just within the reach of existing 8–10 m class telescopes.

REFERENCES

Anders, P., Lamers, H., & Baumgardt, H. 2009, A&A, 502, 817
Ashman, K. M., Bird, C. M., & Zepf, S. E. 1994, AJ, 108, 2348

Bailin, J., & Harris, W. E. 2009, ApJ, 695, 1082
Bassino, L. P., Faifer, F. R., Forte, J. C., Dirsch, B., Richtler, T., Geisler, D., & Schuberth, Y. 2006, A&A, 451, 789
Baumgardt, H., Kroupa, P., & Parmentier, G. 2008, MNRAS, 384, 1231
Baumgardt, H., & Makino, H. 2003, MNRAS, 340, 227
Bedin, L. R., Piotto, G., Anderson, J., Cassisi, S., King, I. R., Momany, Y., & Carraro, G. 2004, ApJ, 605, L125
Blakeslee, J., Cantiello, M., & Peng, E. 2010, ApJ, 710, 51
Blakeslee, J., et al. 2009, ApJ, 694, 556
Boily, C., & Kroupa, P. 2003, MNRAS, 338, 665
Brodie, J. P., & Strader, J. 2006, ARA&A, 44, 193
Caloi, V., & d'Antona, F. 2007, A&A, 463, 949
Cockcroft, R., Harris, W. E., Wehner, E. M. H., Whitmore, B. C., & Rothberg, B. 2009, AJ, 138, 758
Cohen, J. G., Blakeslee, J. P., & Côté, P. 2003, ApJ, 592, 866
Cohen, J. G., Blakeslee, J. P., & Ryzhov, A. 1998, ApJ, 496, 808
Côté, P., Marzke, R. O., & West, M. J. 1998, ApJ, 501, 554
Côté, P., et al. 2004, ApJS, 153, 223 (ACS VCS I)
Côté, P., et al. 2006, ApJS, 165, 57 (ACS VCS VIII)
Côté, P., et al. 2007, ApJ, 671, 1456 (ACS FCS II)
Dirsch, B., Richtler, T., Geisler, D., Forte, J. C., Bassino, L. P., & Gieren, W. P. 2003, AJ, 125, 1908
Dopita, M. A., & Smith, G. H. 1986, ApJ, 304, 283
Fall, M., Krumholz, M. R., & Matzner, C. D. 2010, ApJ, in press (arXiv:0910.2238)
Fan, Z., Ma, J., & Zhou, X. 2009, Res. Astron. Astrophys., 9, 993
Ferrarese, L., et al. 2006a, ApJS, 164, 334 (ACS VCS VI)
Ferrarese, L., et al. 2006b, ApJ, 644, L21
Forbes, D. A., et al. 2010, MNRAS, in press (arXiv:0911.4743)
Forte, J. C., Faifer, F., & Geisler, D. 2007, MNRAS, 382, 1947
Frank, J., & Gisler, G. 1976, MNRAS, 176, 533
Gnedin, O. Y., et al. 2002, ApJ, 568, 23
Harris, W. E. 2009, ApJ, 703, 939
Harris, W. E., Kavelaars, J. J., Hanes, D. A., Pritchet, C. J., & Baum, W. A. 2009, AJ, 137, 3314
Harris, W. E., Spitler, L. R., Forbes, D. A., & Bailin, J. 2010, MNRAS, 401, 1965
Harris, W. E., et al. 2006, ApJ, 636, 90
Hilker, M., Infante, L., & Richtler, T. 1999, A&AS, 138, 55
Humphrey, J. 2009, ApJ, 690, 512
Jordán, A., et al. 2004a, ApJS, 154, 509 (ACS VCS II)
Jordán, A., et al. 2004b, ApJ, 613, 279 (ACS VCS III)
Jordán, A., et al. 2005, ApJ, 634, 1002 (ACS VCS X)

Jordán, A., et al. 2007a, ApJS, 169, 213 (ACS FCS I)
Jordán, A., et al. 2007b, ApJS, 171, 101 (ACS VCS XII)
Jordán, A., et al. 2009, ApJS, 180, 54 (ACS VCS XVI)
Kauffmann, G., White, S. D. M., Heckman, T. M., Ménard, B., Brinchmann, J., Charlot, S., Tremonti, C., & Brinkmann, J. 2004, MNRAS, 353, 713
Kauffmann, G., et al. 2003, MNRAS, 341, 54
Kirby, E. N., Simon, J. D., Geha, M., Guhathakurta, P., & Frebel, A. 2008, ApJ, 685, L43
Kruijssen, D., & Lamers, H. 2008, A&A, 490, 151
Kruijssen, D. 2009, A&A, 507, 1409
Krumholz, M., & Matzner, C. 2009, ApJ, 03, 1352
Lada, C. J., & Lada, E. A. 2003, ARA&A, 41, 57
Lee, Y.-W., Joo, J.-M., Sohn, Y.-J., Rey, S.-C., Lee, H.-C., & Walker, A. R. 1999, Nature, 402, 55
Mei, S., et al. 2007, ApJ, 655, 144 (ACS VCS XIII)
Mieske, S., & Baumgardt, H. 2007, A&A, 475, 851
Mieske, S., et al. 2006, ApJ, 653, 193 (ACS VCS XIV)
Milone, A. P., et al. 2008, ApJ, 673, 241
Morgan, S., & Lake, G. 1989, ApJ, 339, 171
Parmentier, G. 2004, MNRAS, 351, 585
Parmentier, G., & Gilmore, G. 2001, A&A, 378, 97
Peng, E., et al. 2006, ApJ, 639, 95 (ACS VCS IX)
Peng, E., et al. 2008, ApJ, 681, 197
Peng, E., et al. 2009, ApJ, 703, 42 (ACS VCS XV)
Piotto, G., et al. 2005, ApJ, 621, 777
Piotto, G., et al. 2007, ApJ, 661, L53
Recchi, S., & Danziger, I. J. 2005, A&A, 436, 145
Richtler, T. 2005, Bull. Astron. Soc. India (arXiv:astro-ph/0512545)
Schlegel, D. J., Finkbeiner, D. P., & Davis, M. 1998, ApJ, 500, 525
Simon, J., & Geha, M. 2007, ApJ, 670, 313
Sirianni, M., et al. 2005, PASP, 117, 1049
Smith, G. H. 1996, PASP, 108, 176
Spitler, L. R., Larsen, S. S., Strader, J., Brodie, J. P., Forbes, D. A., & Beasley, M. A. 2006, AJ, 132, 1593
Strader, J., Brodie, J. P., Spitler, L., & Beasley, M. A. 2006, AJ, 132, 2333
Strader, J., & Smith, G. H. 2008, AJ, 136, 1828
Tenorio-Tagle, G., Wünsch, R., Silich, S., & Palous, J. 2007, ApJ, 658, 1196
Thoul, A., et al. 2002, A&A, 383, 491
Villanova, S., et al. 2007, ApJ, 663, 296
Waters, C. Z., Zepf, S. E., Lauer, T. R., & Baltz, E. A. 2009, ApJ, 693, 463
Wehner, E. M. H., Harris, W. E., Whitmore, B. C., Rothberg, B., & Woodley, K. A. 2008, ApJ, 681, 1233
West, M. J., Côté, P., Marzke, R. O., & Jordán, A. 2004, Nature, 427, 31
Yoon, S., Yi, S. K., & Lee, Y. 2006, Science, 311, 1129